Original Article

Microstructure and mechanical properties of hot isostatic pressed tungsten heavy alloy with FeNiCoCrMn high entropy alloy binder

Zahid Anwer [a], Malik Adeel Umer [a,*], Fatima Nisar [a], Muhammad Arslan Hafeez [b], Khurram Yaqoob [a], Xian Luo [c], Iftikhar Ahmad [d]

[a] School of Chemical and Materials Engineering, SCME, National University of Sciences and Technology, NUST, Islamabad, Pakistan
[b] School of Materials Science and Engineering, Huazhong University of Science and Technology, 430073, Wuhan, China
[c] State Key Lab of Solidification Processing, Northwestern Polytechnical University, Xi'an 710072, PR China
[d] Center of Excellence for Research in Engineering Materials, Deanship of Scientific Research, King Saud University, Riyadh 11421, Saudi Arabia

ARTICLE INFO

ABSTRACT

Microstructural development and mechanical properties of tungsten heavy alloy, WHA, with FeNiCoCrMn high entropy alloy, HEA, binder were investigated and compared to conventional WHA using Fe−Ni binder. Both WHAs, with HEA and conventional Fe−Ni binders, were fabricated by hot isostatic pressing at a temperature of 1450 °C in an argon environment. Scanning electron microscopy revealed that WHA with HEA and conventional binders possessed uniform and well-refined microstructures. Energy dispersive spectroscopy and X-ray diffraction, XRD, spectroscopy validated the formation and composition of HEA, existing as a skeletal network surrounding tungsten grains. HEA binder exhibited an overall increase of 42% in micro Vickers hardness values. Furthermore, hardness values of the tungsten heavy alloy were also seen to rise when fabricated with HEA binder. However, WHA sample with HEA binder was seen to undergo faster strain hardening and a premature failure, leading to lower values of ultimate strength and reduced ductility.

* Corresponding author.
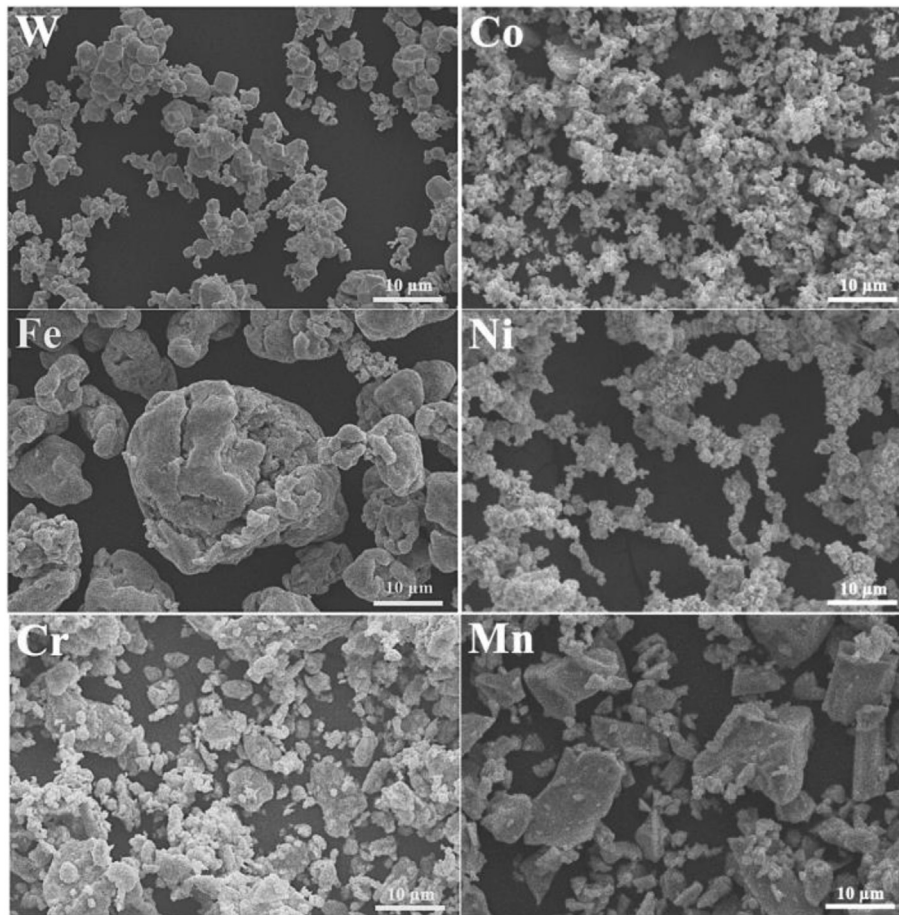 E-mail address: umer.adeel@scme.nust.edu.pk (M.A. Umer).

Fig. 1 − **SEM micrographs of the elemental powders used for the fabrication of WHAs.**

1.   Introduction

Tungsten heavy alloys (WHAs) are two-phase alloys, composed of greater than 85 wt% hard spherical tungsten particles embedded in a ductile matrix [1]. WHAs are extensively used in ballistic applications, plasma-facing components [2], aircraft counter balances, radiation shields, ballasts, vibration-damping devices, and ordinance applications (kinetic energy penetrators and pre-fragments) [3] due to their superior mechanical properties [4], higher density (17−18 g/cm^3) [3], high erosion-resistance, high melting point, excellent thermal conductivity, low sputtering, high structural integrity, better endurance limit, and significant radiation shielding [2]. To further widen their field of applications, it is mandatory to further improve their mechanical properties particularly strength and toughness [5].

In the last few years, vigorous research has been conducted on the improvement of mechanical properties of WHAs by various techniques, including exploration of new powder synthesis techniques [6,7], alloying elements and new binders addition [8−10], post-sintering plastic deformation strengthening techniques [11−13], high energy milling of powders [14,15], microstructure refinement [16−18], cold deformation [19,20], and nano-sized particles strengthening [21]. Among all, alloying elements and new binder addition is one of the easy, cost-effective, and widely used methods of improving mechanical properties. Various binders, such as 10% Fe−Ni [22], rare earth oxide particles (Y_2O_3, La_2O_3, and CeO_2) [23], nano-sized ZrO_2, 4.9Ni−2.1Fe [5], pure nickel [24], and recently high entropy alloys (HEAs) [25] have been used to improve the mechanical properties of WHAs.

HEAs are a new class of materials, comprising of five or more elements in near equimolar ratio. The significantly increased entropy of the system facilitates the formation of a single-phase solid solution [26−28]. HEAs with a face-centered cubic (FCC) structure cause a significant improvement in impact toughness of the brittle tungsten phase. Phase formation in HEA depends on different solid solution formation criteria, including valence electron concentration (VEC), atomic size difference (δ), and enthalpy (ΔH_{mix}). Solid solution formation is favorable when ΔH_{mix} lies between −15 <ΔH_{mix}<5 kJ/mol and delta (δ) < 6.6%, whereas VEC> 8 favors the formation of FCC structure [29,30]. Moreover, HEAs also have the potential to improve penetration or self-sharpening ability and mechanical properties of WHAs, when embedded as a binder [31,32]. Some HEAs, including CoCrFeCuMn, and AlCoCrCuFeNi, have been reported as binders in WHAs [33,34].
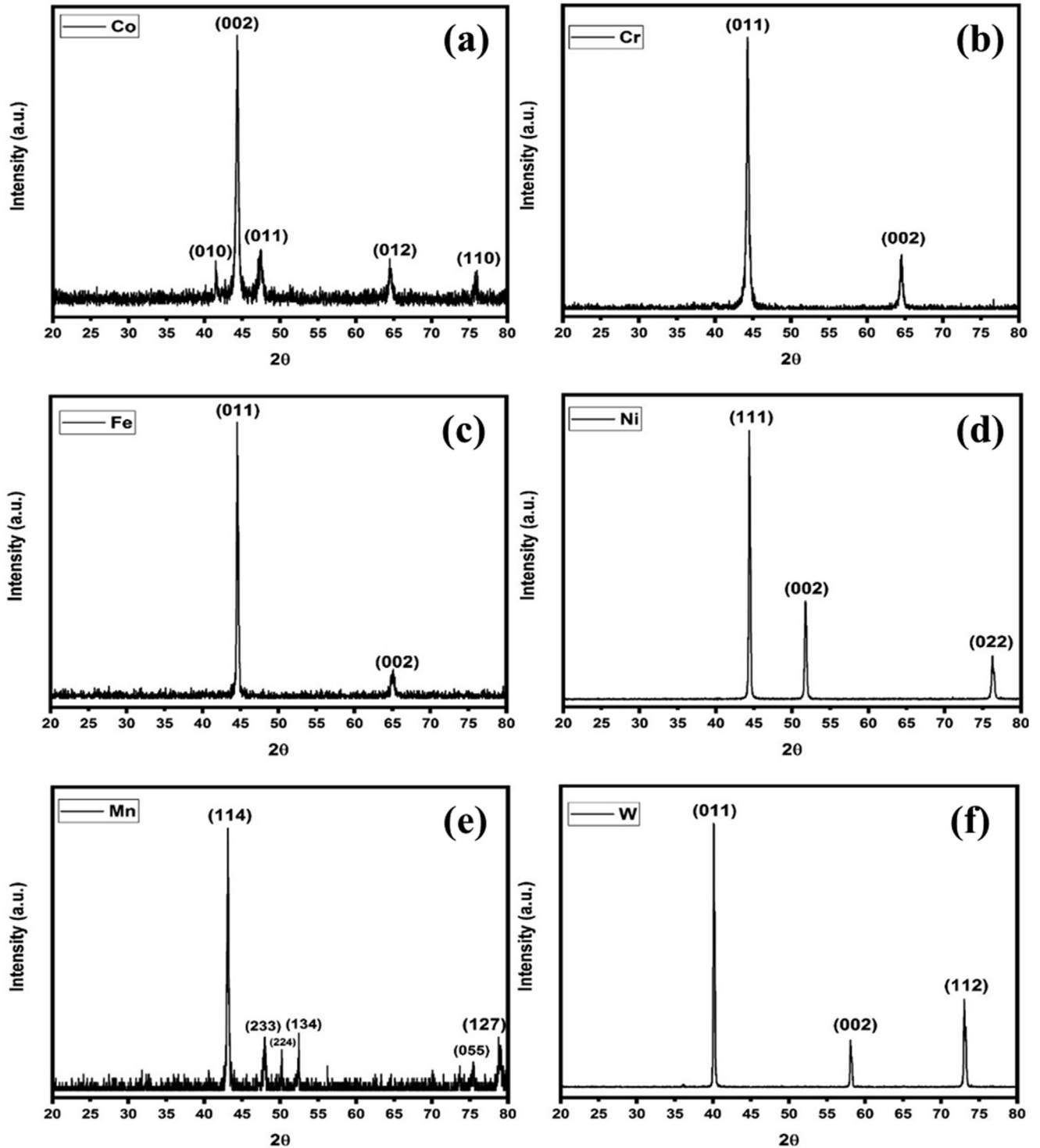
Fig. 2 − XRD spectra of (a) Co, (b) Cr, (c) Fe, (d) Ni, (e) Mn, and (f) W powders, used for fabrication of HEA-WHA and Con-WHA.

This work aims to investigate the microstructure and mechanical properties of WHA with FCC FeNiCoCrMn HEA binder (HEA-WHA), fabricated by hot isostatic pressing (HIP) in comparison to conventional WHA with Fe−Ni binder (Con-WHA). The results of scanning electron microscopy (SEM), energy dispersive spectroscopy (EDS), and X-ray diffraction analysis (XRD) were obtained to evaluate the microstructures of HIP processed WHAs. Their mechanical properties were also evaluated by the micro Vickers hardness and compression tests.

2.   Experimental procedures

2.1.   Materials and their characterization

Co, Cr, Fe, Ni, Mn, and W powders of purity 99%, and mesh size 120 were purchased from Chengdu Best New Materials Co. Ltd. China and used as received. The morphologies, used for the measurement of particle size, of all powders were analyzed through SEM (*Tescan Vega3, France*) at 2000 × magnification as illustrated in Fig. 1, whereas the purity of all powders was validated by XRD analysis, performed on X-ray diffractometer (*STOE Theta/Theta, Germany*) equipped with fluorescence and K_β radiation filters, using CuK_α radiations (λ = 1.5418 Å). The diffraction patterns were obtained through a step scan mode (step size 0.020, scan rate 0.1sec) in the 2θ range of 20°−80°. The obtained XRD spectra are presented in Fig. 2.

The particle sizes of Co, Cr, Ni, and W were observed to be in the range of 2.5−3 μm and that of Fe and Mn in the range of 5−10 μm. It was observed that Co and Cr particles possessed a solid irregular shape. On the other hand, Fe particles were observed to have a nearly spherical shape, Ni particles have a porous/spongy shape, Mn particles have sharp-edged morphology, and W particles have a polygonal shape. Having particles of nearly same sizes increases mixing efficiency and ensures better dispersion, prior to any sintering or heat-treatment. It has been reported that the powders with similar average particle sizes facilitate the homogeneity of mixing and promote better alloying during the sintering cycle [35].

In our study, using binder powder of similar size is believed to have favored a more homogenous alloy formation. XRD spectra validated the originality of all Co, Cr, Fe, Ni, Mn, and W powders negligible impurity levels by demonstrating intensity peaks (002), (011), (011), (111), (114), and (011), respectively (Fig. 2).

2.2.   Powder mixing and cold isostatic pressing

For the fabrication of both HEA-WHA and Con-WHA, Co, Cr, Fe, Ni, Mn, and W powders were weighed in equimolar ratios as per calculations on a weighing balance (Sartorius GC−1603 P Germany with an accuracy of 0.0002 g). To promote the formation of face-centered cubic crystal structure in HEA, equimolar ratios of Co, Cr, Fe, Ni, and Mn that were taken are tabulated in Table 1. All powders were mixed at room temperature in a powder mixer (Hermann Dusseldorf SO HN; Type IMG 200, Germany) for 30 min at a mixing speed of approximately 150 rpm.

The powder mixtures were then pressed through cold isostatic pressing (*Viv Tek, CIP T20-E, USA*) into cylindrical green compacts of length 50 mm and diameter 40 mm under a

pressure of 150 MPa for 1 min. The green compacts of chemical compositions given in Table 1 and green densities, ranging from 70 to 73% of the theoretical density, were obtained.

2.3.   Hot isostatic pressing

The green compacts were then sintered by the HIP process, using HIP furnace (*PVA TePla-AG, Type COD 533 R, Germany*). The process began with the heating of green compacts at a rate of 5 °C/min to 1150 °C temperature. After 1150 °C temperature, samples were further heated 1450 °C at a relatively slow heating rate of 3 °C/min. The samples were first soaked at 1450 °C for 60 min and then subjected to HIP for 30 min under high argon gas pressure of 30−45 bars. After HIP, the samples were first slowly cooled to 1000 °C at a cooling rate of 3 °C/min and then rapidly cooled to room temperature at a cooling rate of 20 °C/min. Finally, the HIP pressed samples were cleaned for subsequent characterization. The schematic of the complete HIP process is illustrated in Fig. 3.

2.4.   Microstructure analysis

The microstructures of both the fabricated HEA-WHA and Con-WHA were examined on SEM (*Tescan Vega3, France*). The sintered samples were sectioned by electrical discharge machine (*High precision AR-50 CNC EDS, China*) into samples of diameter 11 mm and thickness 3 mm. These samples were then manually ground on silicon carbide grinding (SiC) papers of grades P200, P400, P600, P800, P1000, and P1500, polished on velvet and nylon cloths with diamond paste (1 and 0.25 μm) using an automatic polisher (*Ecomet 250 Grinder/Polisher USA*) and etched in 2 : 1 solution of H_2SO_4 and HNO_3. Before microstructural examination samples were sputter-coated with gold (purity 99.99%, thickness 15 nm) to obtain high-quality micrographs at 880 × magnification. Elemental analysis was also carried out, using EDS equipped with new generation silicon drift detector (SDD) attached with SEM through spot analysis technique by selecting spots at both binder and tungsten portions. Phase analysis was also performed on an X-ray diffractometer (*STOE Theta/Theta,*

Table 1 − Chemical compositions of both Con-WHA and HEA-WHA (wt%).

Sample	Co	Cr	Mn	Ni	Fe	W
Con-WHA	1.614	1.423	1.526	1.614	1.525	92.3
HEA-WHA	0.3	—	0.5	4.20	2.50	92.5
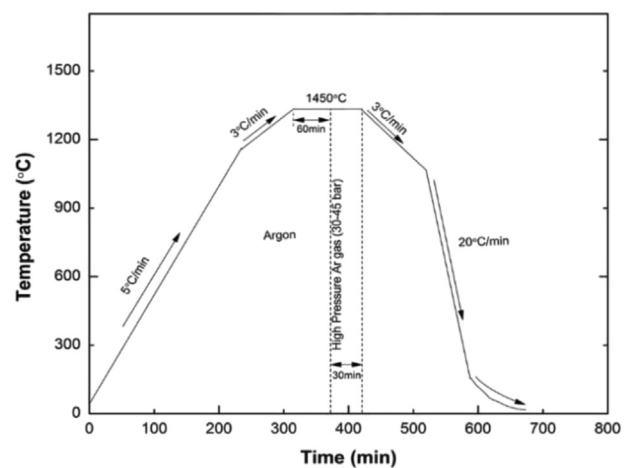
Fig. 3 − Schematic of HIP cycle under argon gas, used to fabricate both HEA-WHA and Con-WHA.

Germany) equipped with fluorescence and K_β radiation filters, using CuK$_\alpha$ radiations (λ = 1.5418 Å). The diffraction patterns were obtained through a step scan mode (step size 0.020, scan rate 0.1sec) in the 2θ range of 20°–80°. The relative densities of the fabricated samples were measured employing the Archimedes principle using an analytical weighing scale with density kit (*WT3003GHS, WANT, China*).

2.5. Mechanical testing

Hardness testing of both HEA-WHA and Con-WHA was conducted on micro Vickers hardness tester (*Tinius Olsen, FH-006, UK*) equipped with diamond indenter, under the load of 0.98 N and 9.8 N as per ASTM E92 standard. A dwell time of 10s was kept, with five readings noted for each sample and averaged to get the final hardness value. For compression testing of fabricated WHAs, samples dimension and testing procedure, mentioned in ASTM B-925 standard, were followed. Compression testing was performed on a universal testing machine (*Tinius Olsen, Super 602L, UK*) equipped with an extensometer and 300 KN load cell at a strain rate of 0.127 mm/min.

3. Results and discussion

3.1. Analysis of HEA by thermodynamics

The analysis of fabricated HEA was carried out, using solid solution formation criteria. For this purpose, first entropy of mixing (ΔS_{mix}) was calculated by Eq. (1) [27]

$$\Delta S_{mix} = -R \sum_{i=1}^{N} x_i \, ln \, x_i \tag{1}$$

Where, x_i is molar ratio of ith element, N is the number of elements, and R is universal gas constant. Secondly, the enthalpy of mixing (ΔH_{mix}) was calculated by Eq. (2) [27]

$$\Delta H_{mix} = \sum_{i=1,i\neq j}^{N} 4\Delta H_{AB}^{mix} x_i x_j \tag{2}$$

Table 2 – Calculated parameters for FeNiCoCrMn HEA by thermodynamics.

Entropy (J/K)	Enthalpy (kJ/mol)	δ (%)	VEC	Melting Point (°C)	Ω
13.37	−1.56	1.66	8.06	1525	15.43

Where, ΔH_{AB}^{mix} is the enthalpy of mixing of element A and B. Thirdly, the atomic size difference (δ) was calculated by Eq. (3) [27]

$$\delta = \sqrt{\sum_{i=1}^{N} x_i \left(1 - \frac{r_i}{\bar{r}}\right)^2} \tag{3}$$

Where, r_i is the atomic radius of ith element and $\bar{r}$ is as follows: $\bar{r} = \sum_{i=1}^{N} x_i r_i$. After that valence electron concentration (VEC) was calculated by Eq. (4) [27]

$$VEC = \sum_{i=1}^{N} x_i VEC_i \tag{4}$$

where, VEC_i is the number of valence electrons of ith element. Finally, to accommodate the opposite effects of the enthalpy and entropy, the Ω was calculated by Eq. (5) [27], which gave a tradeoff between the two quantities

$$\Omega = \frac{T_m \Delta S_{mix}}{|\Delta H_{mix}|} \tag{5}$$

Where, T_m is the melting point. Calculated values of all parameters are tabulated in Table 2.

The ΔS_{mix} slightly exceeded the minimum value of 13 and ΔH_{mix} fell within the brackets of −15 and 5 kJ/mol, which restricted the intermetallic formation. δ and VEC were calculated to be 1.66% and 8.06 respectively, suggesting the feasibility of substitution and facilitated the formation of FCC solid solution. Both enthalpy and entropy accounted for the decrease in Gibb's free energy and phase stability in alloys therefore, it was important to introduce a parameter Ω, which gave a trade-off between the two quantities. If the effect of entropy dominated enthalpy of mixing at melting
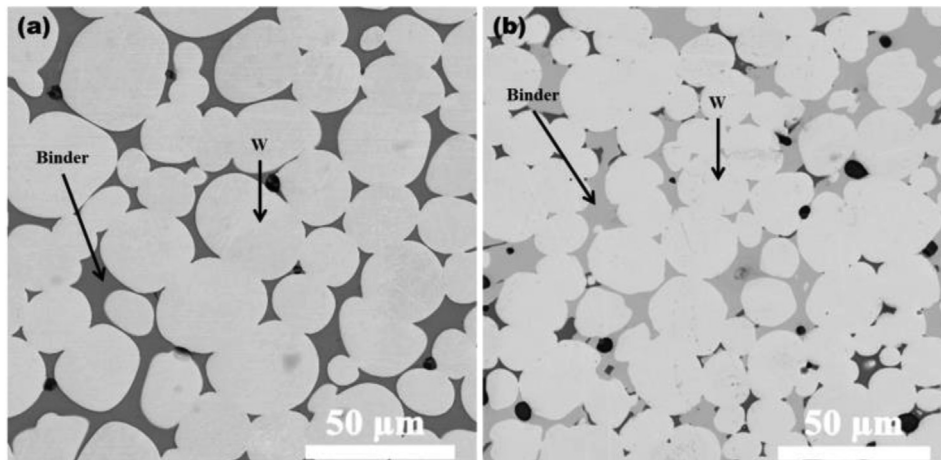
Fig. 4 – SEM micrographs of (a) Con-WHA and (b) HEA-WHA, fabricated by HIP process.

Table 3 – Microstructural parameters of Con-WHA and HEA-WHA.

Sample	W mean size (μm)	Contiguity	Density (g/cm³)
Conventional WHA	20.86	0.34	17.65
HEA-WHA	16.13	0.42	17.50

temperature, the ratio turned out to be greater than 1, which implied that the criteria for solid solution formation in HEA has been fulfilled. The value of Ω came out to be 15.43, as shown in the table, suggesting a dominating effect of entropy over enthalpy of mixing. Hence, it can be concluded that FeNiCoCrMn, theoretically, is expected to form a single-phase solid solution.

3.2. Microstructure

Backscattered mode SEM micrographs of both HEA-WHA and Con-WHA, fabricated by the HIP process are illustrated in

Fig. 4, whereas the corresponding EDS and XRD spectra are presented in Figs. 6—8. It can be observed that both Con-WHA and HEA-WHA exhibited sufficiently dense and uniform microstructures with homogenously distributed tungsten particles within the binder matrix, as illustrated in Fig. 4.

The entire densification process in liquid phase sintering has been classified into three distinct stages, i) re-arrangement or liquid spreading ii) solution re-precipitation and iii) grain growth [36]. Tungsten, being the heavier element, appears to have bright, round grains embedded into a darker, grey interconnected network of the binder. In both the images, a round morphology of tungsten grains can be
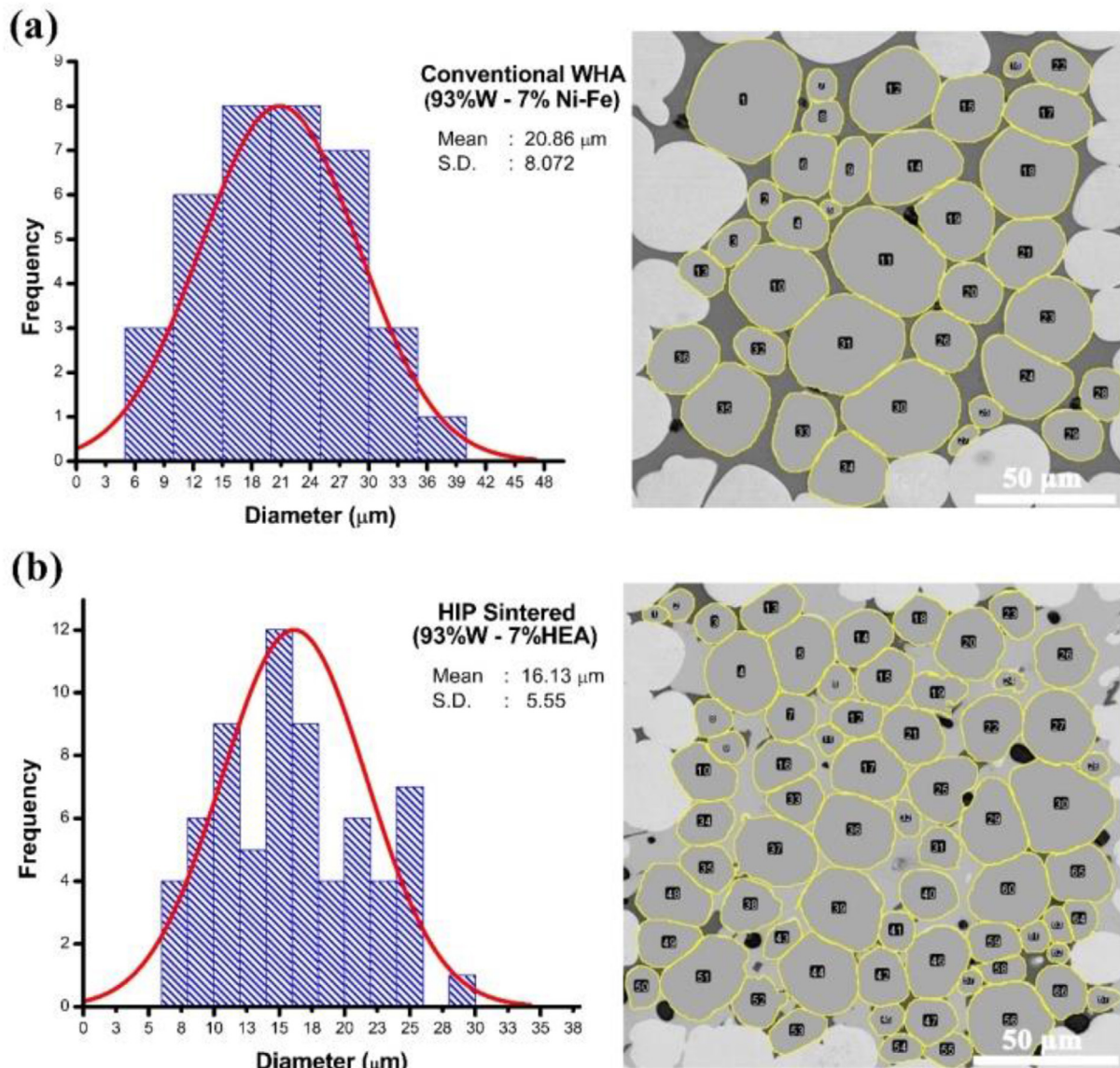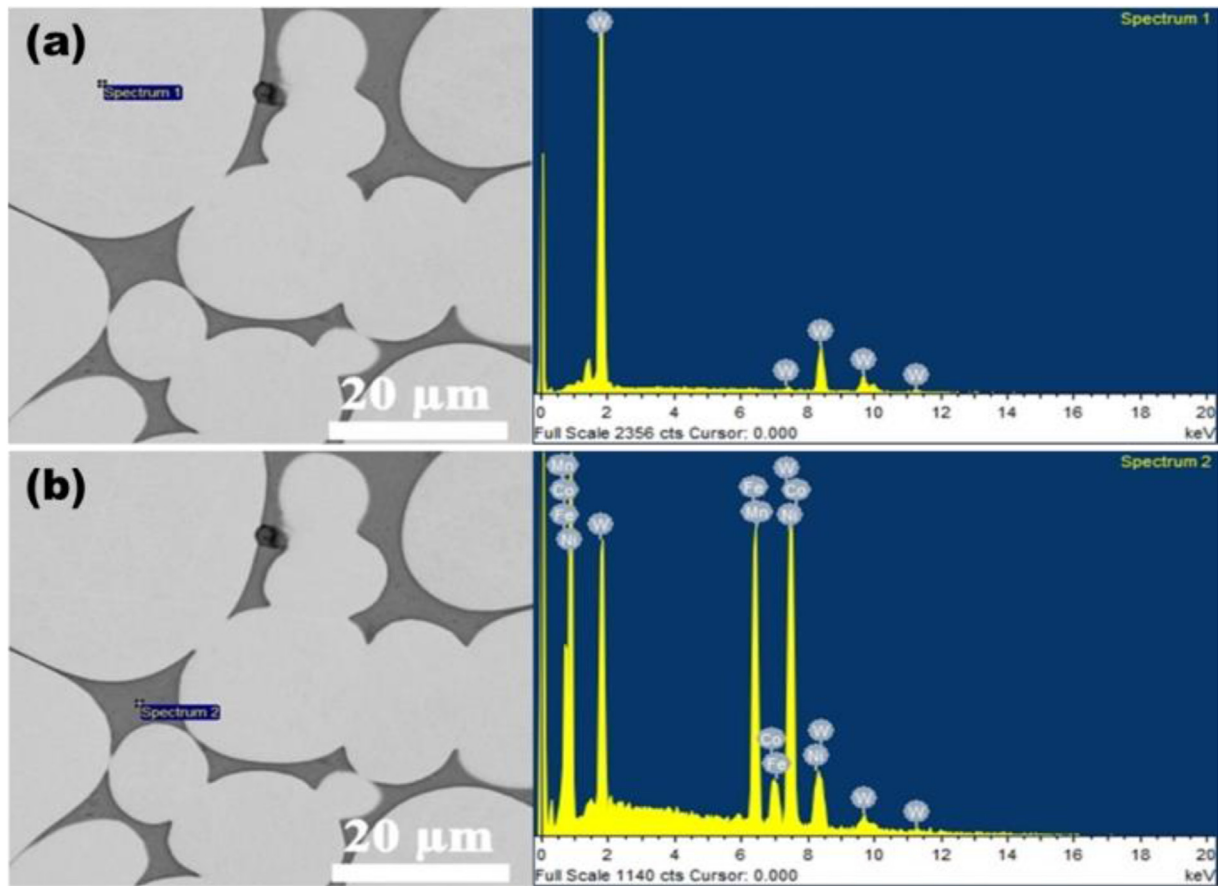

Fig. 5 – Particle size distribution normal curve (a) Conventional WHA and (b) HEA-WHA.
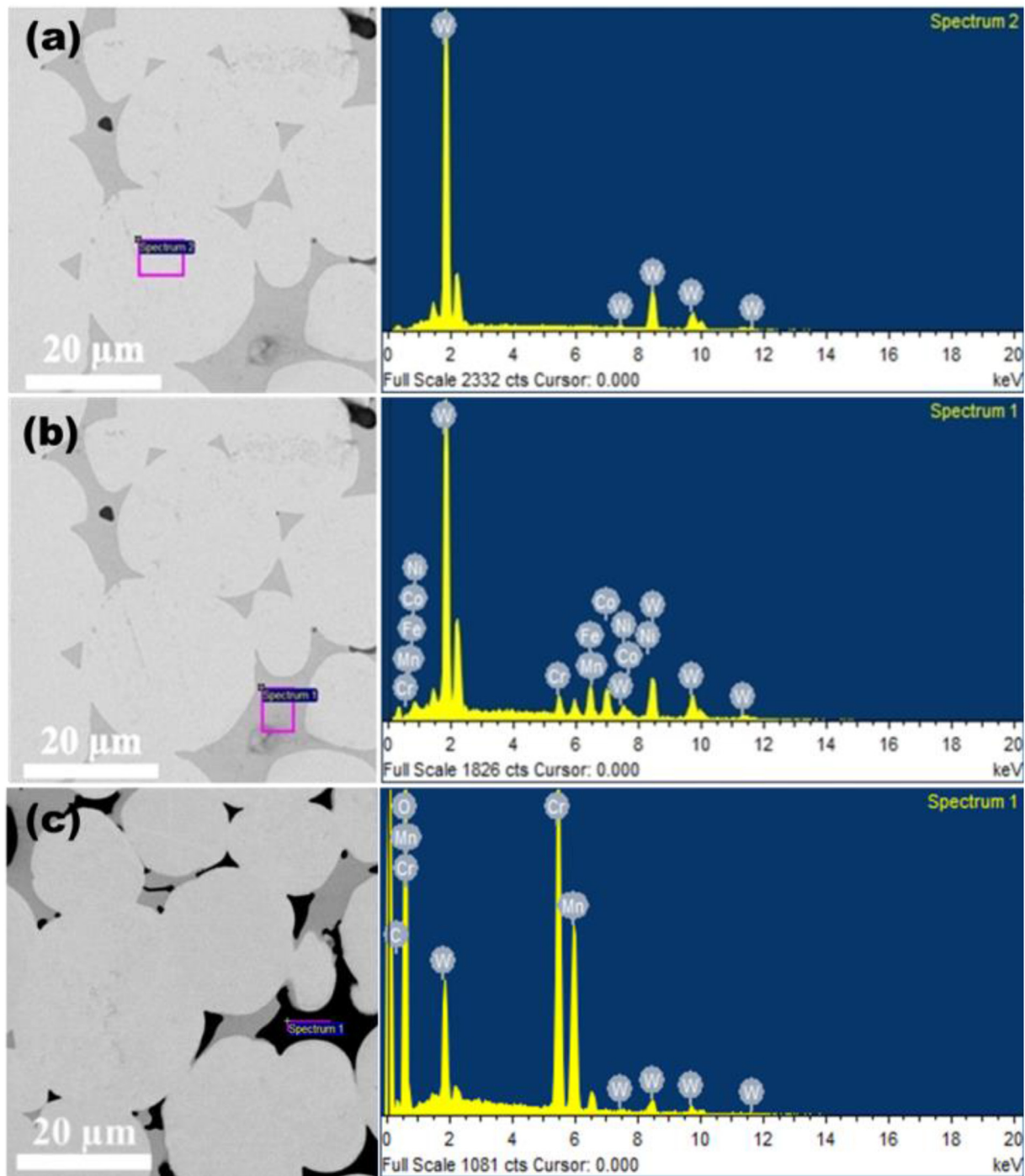
Fig. 6 − EDS spectra of Con-WHA, performed by selecting spots at (a) W portion and (b) FeNi based binder portion, fabricated by HIP process.

seen to exist in the binder network, suggesting the occurrence of solution re-precipitation followed by grain growth. This is vital to the fabrication of highly dense composite materials through the liquid phase processing as it ensures densification and formation of a sound interface between the matrix and the binder [37]. The liquid is formed by melting of binder elements with lower melting points than the tungsten particles. This liquid, which usually has solubility for tungsten atoms, wets the W particles and starts filling the pores by means of capillary forces thereby, reducing the interfacial energies. This process is known as rearrangement in which, the liquid starts to dissolve tungsten around the interfacial areas; rendering the W particles a more rounded shape unlike the pure particles shown in Fig. 1. There is quite a deviation from the initial particle size of tungsten which was measured to be roughly 2 μm. The application of pressure during HIP greatly contributes to the densification of these alloys by enhancing sintering kinetics and a pressure aided filling up of pores by the liquid binder [38]. Similar results have recently been published, which report highly dense WHA with HEA binder when using pressure assisted spark plasma sintering (SPS) route [39]. Along with the presence of W and binder, Fig. 4(b) also reveals the presence of discretely present tiny black spots in the HEA-WHA microstructure which appear

circular in shape and are seen to exist typically at the grain junctions. These can be classified as regions of porosity which are observed in both types of alloys, more in the HEA-WHA sample.

The tungsten grain size distribution presented in Fig. 5 indicates a finer grain structure of HEA-WHA with low value of standard deviation. On the other hand, the size distribution of Con-WHA reveals a relatively coarser structure with high value of standard deviation, indicating an optimal progression of the liquid phase sintering process with a higher amount of smaller grains being dissolved and re-precipitated on to larger ones.

Table 3 compares some key parameters between the two alloys. Apparent density values of the Con-WHA have been measured to be slightly higher than those of HEA-WHA, leading to the conclusion that HEA-WHA have more porosity in them. Lower density values could also arise from the formation of oxide particles in HEA-WHA, discussed in the later stage(s) of the manuscript. Higher contiguity and a lower mean size of HEA-WHA indicates that the processes of solution re-precipitation and grain growth progressed in a relatively slower manner. A low W diffusion coefficient in HEA binder and the sluggish diffusion effect in high entropy alloys are the main reasons responsible for these differences. The

Fig. 7 — EDS spectra of Con-WHA, performed by selecting spots at (a) W portion and (b) Fe—Ni binder portion, fabricated by HIP process.

effect of sluggish diffusion in HEAs on microstructure and mechanical properties has now been extensively studied and reported [40]. The process of solution re-precipitation and grain growth in WHAs requires W to have good solubility in the binder. This allows W atoms to diffuse into the binder and re-precipitate on grains with a more rounded curvature, hence the grains which are larger than the average grain size. In the final stages of liquid phase sintering, W grains experience an inhomogeneous change in microstructure where small grains

preferentially dissolve and large grains experiencing growth, leading to an overall reduction in the system's interfacial energy. The kinetics of this process is largely dependent on the diffusion coefficient of W in the binder system. The presence of five principle elements in FeNiCoCrMn HEA, is expected to result in reduced values of W diffusion coefficient thereby, reducing the overall mobility of W atoms in them. Overall, W grain growth process is decelerated, rendering a finer W grain size than conventional WHAs. The microstructural difference
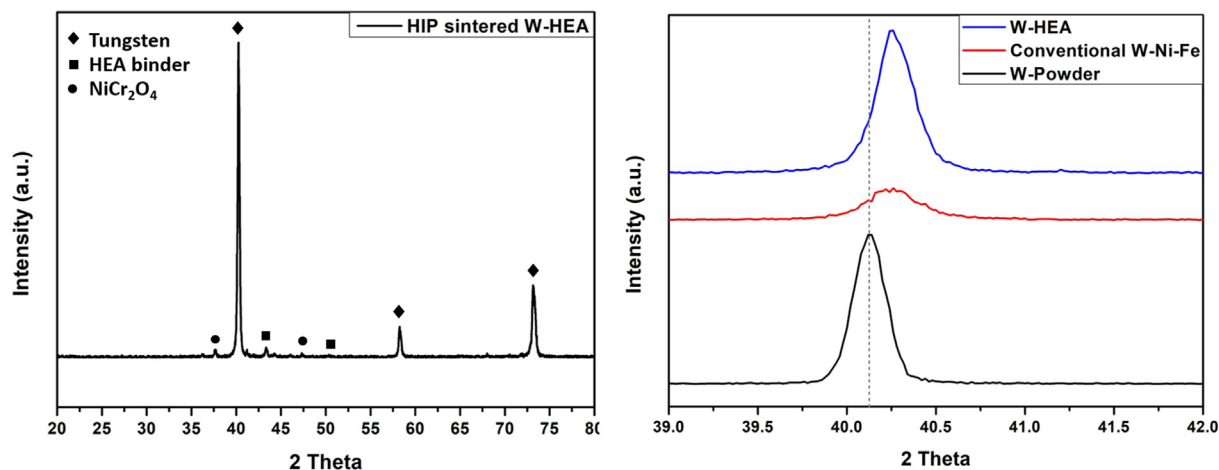
Fig. 8 — (a) XRD spectrum of HEA-WHA and (b) stacked XRD spectra of W powder, HEA-WHA and Con-WHA, presenting peak shifts.

is represented by lower values of mean size and deviation of W grains in HEA-WHA. In liquid phase sintering, the grain growth rate constant depends on diffusion in the liquid phase, which can be expressed as [41]:

$$K = \frac{64\, D_S\, C\, \Omega\, \gamma_{SL}}{9\, RT} \qquad (6)$$

where K is the grain growth rate constant, D_S is the solid diffusivity in the liquid, C is the solid solubility in the liquid, γ_{SL} is the solid-liquid surface energy, R is the gas constant, T is the absolute temperature, and Ω is the molar volume of W. Because the dihedral angle in W-HEA and W—NiFe is ~66° and ~50°, respectively, γ_{SL} in WHEA is ~8% higher than that in

W—NiFe. Thus, γ_{SL} in WHEA contributes to a K value about 8% higher than that in W—NiFe. The solubility of W in the HEA matrix, C, is ~4 at. %, which is ~40% of the solubility in NiFe matrix [42], Considering that the value of K in W-HEA is only 20% of that in W—NiFe, D_S in W-HEA is calculated to be about 46.3% of that in W—NiFe. Consequently, the smaller value of D_S and C in the HEA matrix result in a slower W grain growth rate compared with the conventional W—NiFe. Similar microstructure resulting through conventional liquid phase sintering employing W with HEA binder has been reported [43].

EDS analysis of the obtained microstructure for Con-WHA can be seen in Fig. 6. Two different points were
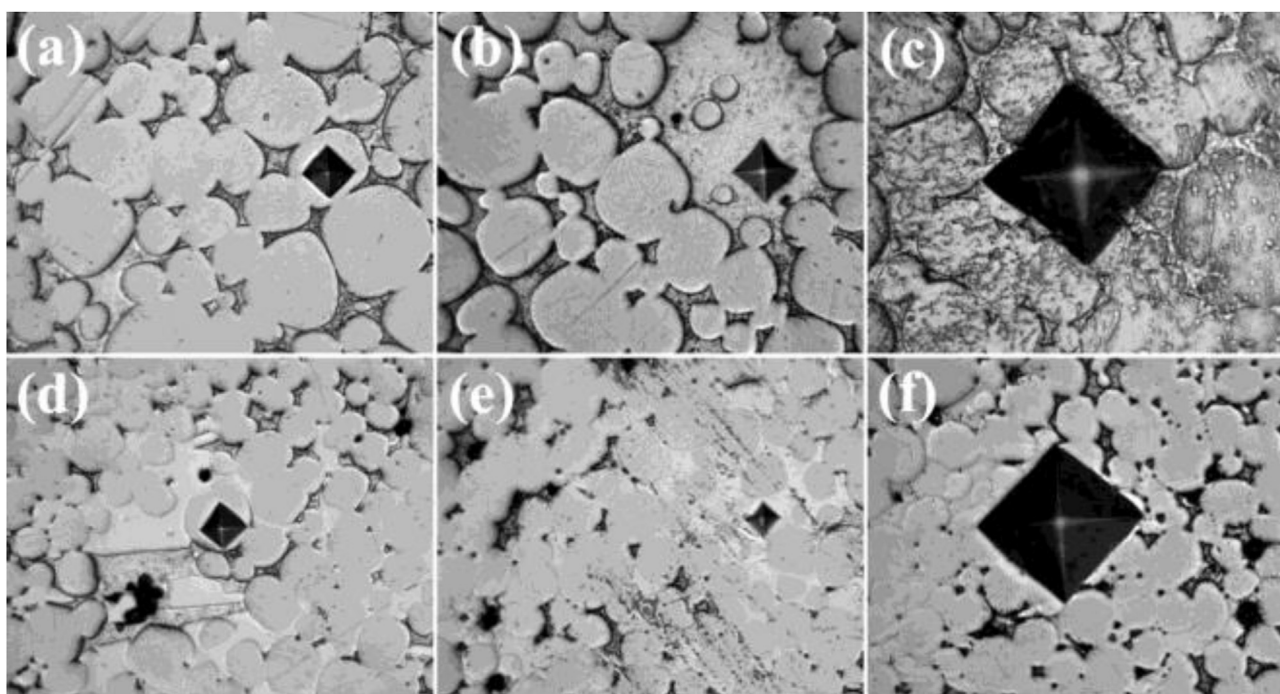

Fig. 9 — Microphraphs with indents, obtained after Vickers hardness test at HV0.98 and HV9.8 of Con-WHA at (a) W portion, (b) binder portion, (c) HV9.8 and HEA-WHA (d) W particle, (e) binder particles, (f) HV9.8.

Table 4 − Micro Vickers hardness values of HEA-WHA and Con-WHA.

Sample	HV/0.98		HV/9.8
	W Particles	Binder	
HEA-WHA	528.14	570.83	456.75
Con-WHA	398.37	261.08	322.00

taken for the EDS scan, corresponding to Fig. 6(a) W grain and Fig. 6(b) binder rich region. Peaks corresponding to Fe, Ni, Co and Mn can be seen in Fig. 6(b), confirming the presence of all these elements in the binder phase. EDS spectrum in Fig. 7(b) validates the presence of all five constituents of the HEA binder. Due to the large volume nature of EDS scan and the geometric factors that modify X-ray generation and propagation, resulting in non-systematic variations in the actual percentages of different elements, EDS values are best kept for identification and qualitative purposes. The results in Fig. 7(c) correspond to the dark regions in the HEA-WHA microstructure which are not porosities. Here, as seen from the elemental scan, Cr and Mn are detected in the presence of oxygen suggesting the formation of oxides of the element(s). The root of the oxide formation lies in the mixing and handling of powder during its processing whereby the powder exposed to the presence of atmospheric oxygen can lead to the formation of extremely fine layer of oxide on the powder surface of reactive elements. These oxides are stable at the sintering conditions and can segregate and/or coalesce at W grain boundaries during the liquid phase sintering process. From the scan it can be inferred that the oxide region would primarily belong to Cr, due to its high oxidation susceptibility under ambient conditions. However, the presence of such oxides can be consequential to the mechanical properties of WHAs, as discussed in proceeding section(s).

The XRD patterns shown in Fig. 8(a) contain peaks that match with the standard elemental tungsten powder and the binder to an FCC based FeNiCoCrMn high entropy alloy [40]. Since the binder was present in a much smaller quantity than tungsten, the diffraction pattern is dominated with peaks corresponding to W. Pure W has a BCC lattice with the first three peaks corresponding to planes (110), (200), and (211) at 40.41°, 58.35°, and 73.33° two-theta respectively. It can be seen that a slight (110) peak shift occurs towards higher angle in the case of HEA-WHA and Con-WHAs, seen in Fig. 8(b), suggesting a decrease in inter-planar spacing due to the formation of substitutional solid solution with the binder element(s) in W lattice. The formation of a solid solution can give rise to the enhancement in mechanical properties of WHAs through solid solution hardening.

3.3. Micro vickers hardness

For hardness measurement, indentation tests were performed under different testing conditions to obtain the hardness of all phases separately. A load of 0.98 N was applied for 10 s to evaluate the hardness of tungsten and binder phase individually, whereas combined hardness values of HEA-WHA and Con-WHA were measured under a load of 9.8 N, illustrated in Fig. 9. The measured hardness values under different loads are tabulated in Table 4.

High entropy alloys have some unusual properties, unique to their structures and compositions, for example, high low and elevated temperature hardness, high strength at elevated temperatures, high wear and corrosion resistance, and a number of other characteristics. It is noted that HEAs with the BCC lattice have predominantly high strength and low ductility, while the FCC based HEAs have relatively low strength but increased ductility. However, the strength of HEAs with the FCC lattice is considered far more superior than their elemental constituents or conventional alloys. The FCC based HEA binder in WHAs is considered to impart strength while providing the necessary ductility required of kinetic penetrators. In results tabulated in Table 4, the HEA binder can be seen exhibiting much superior microhardness values on average, over twice as high than the conventional binder system. The higher hardness values of the HEA binder arise from the much studied extensive solid solution formation in high entropy alloys [33]. Furthermore, it can be seen that W phase in HEA-WHA also displayed a 33% higher hardness value than W phase in Con-WHA. This can be attributed to the difference in microstructure between the two alloy systems. Hardness is quantified primarily as the restriction to dislocation movement at the surface. The presence of certain microstructural factors, such as point defects, dislocation density and strain hardening, stacking faults, grain boundaries, microscopic precipitates and reinforcements, to name a few, restrict dislocation movement thus serving to increase hardness and strength. HEA-WHAs, having a much finer grain structure with the stress fields generated by the diamond indenter in close proximity to the W grain boundary region, in comparison to Con-WHA, result in a readily impediment of dislocation movement culminating in higher hardness values. It is for primarily similar reasons that we find the values of HEA-WHA to be higher for macro-hardness testing as well.
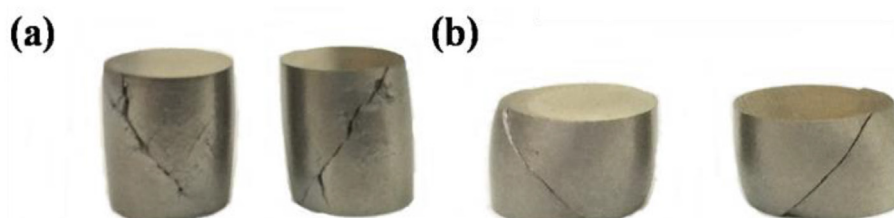
Fig. 10 − Samples obtained after compression testing of HEA-WHA and Con-WHAs.
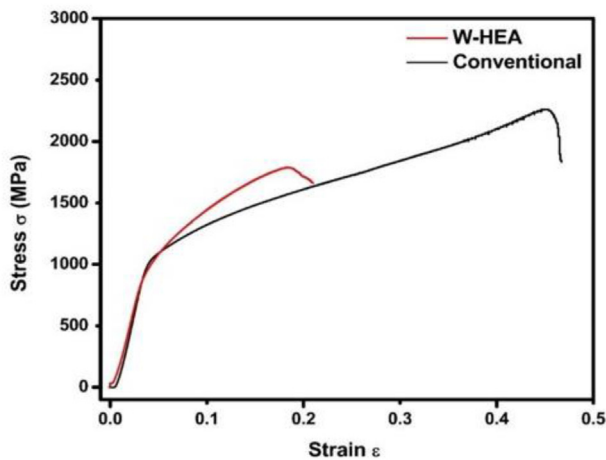
Fig. 11 — Stress-strain curves obtained after compression testing of HEA-WHA and Con-WHA.

3.4. Compressive properties

Samples of both HEA-WHA and Con-WHA, obtained after compression testing, are illustrated in Fig. 10. Stress versus strain curves, for both WHAs, are plotted in Fig. 11, whereas the obtained compressive properties, including ultimate compressive strength, and yield strength are tabulated in Table 5.

HEA-WHA demonstrated a relative brittle fracture as presented by multidirectional crack propagation and branched network on the fractured surface in Fig. 10(a). On the other hand, Con-WHA exhibited ductile fracture as presented by unidirectional crack propagation in Fig. 10(b). This fact can also be depicted by the height of the deformed samples or the total strain experienced through Fig. 11. The tolerance/endurance limit and plastic deformation of Con-WHA was observed to be much greater than that of HEA-WHA.

Due to a relative brittle behavior under compressive load, HEA-WHA exhibited 21% lower ultimate strength and similar value of yield strength when compared to Con-WHA. FCC based FeCrCoNiMn based HEAs are known to exhibit high strengths at room and elevated temperatures [44]. Several factors come into play when determining the behavior of a metal/alloy in the plastic zone. The mechanical response of WHA depends on its microstructure and the deformation aspects of the binder in the plastic zone. The higher strain hardening coefficient of HEAs as compared to their elemental counterparts and a finer grain structure generally leads to higher strain hardening rates [45], as verified in Fig. 11. The microstructure of HEA-WHA was observed to be finer than Con-WHA however, the small amount of oxide formation

during HIP sintering also acts as a reinforcement and barrier towards the motion of dislocations, resulting in a higher strain hardening of HEA-WHA. This can also be validated through the total strain to failure values plotted in Fig. 11 where the presence of porosity, in addition to oxide regions, played a major role in the premature failure of HEA-WHA samples.

4. Conclusions

Following conclusions can be extracted from this work:

- The incorporation of HEA as binder to WHA led to a finer microstructure than conventional FeNi based alloy, which led to improvements in hardness values and strain hardening coefficient.
- A 42% increase in micro-Vickers hardness was observed in HEA-WHA, compared to the Con-WHA.
- Multidirectional crack propagation and branched network on the fracture specimen presented the brittle nature of fracture in HEA-WHA, whereas unidirectional crack propagation on fracture surface presented the ductile fracture of Con-WHA.
- A higher strain hardening coefficient in HEA-WHA promotes self-sharpening abilities and could improve the penetration performance of WHA kinetic penetrators. Consequently, HEA-WHA can serve as a viable replacement for depleted uranium alloys.
- The results presented in this manuscript point to the fact that there is considerable room for further research on the microstructural optimization and mechanical response of HEA based WHAs, in view of binder systems that present lower oxidation and higher sintering kinetics.

Declaration of competing interest

The authors declare that they have no known competing financial interests or personal relationships that could have appeared to influence the work reported in this paper.

REFERENCES

[1] Jian R, Wang L, Zhou S, Zhu Y, Liang YJ, Wang B, et al. Achieving fine-grain tungsten heavy alloys by selecting a high entropy alloy matrix with low W grain growth rate. Mater Lett 2020;278:128405.

[2] Sattar H, Jielin S, Ran H, Imran M, Ding W, Gupta PD, et al. Impact of microstructural properties on hardness of tungsten heavy alloy evaluated by stand-off LIBS after PSI plasma irradiation. J Nucl Mater 2020;540:152389.

[3] Kiran UR, Prabhu G, Nandy TK. Cooling rate effects on microstructure and mechanical behaviour of tungsten heavy alloys. Mater Today Proc 2020;26:1631—7.

[4] Hafızoğlu H, Durlu N. Effect of sintering temperature on the high strain rate-deformation of tungsten heavy alloys. Int J Impact Eng 2018;121:44—54.

Table 5 — Compressive properties of HEA-WHA and Con-WHA.

Samples	Ultimate Strength (MPa)	Yield Strength (MPa)	Total Strain
HEA-WHA	1788	972	0.210
Con-WHA	2250	1005	0.467

[5] Xu L, Xiao F, Wei S, Zhou Y, Pan K, Li X, et al. Development of tungsten heavy alloy reinforced by cubic zirconia through liquid-liquid doping and mechanical alloying methods. J Refract Met Hard Mater 2019;78:1-8.

[6] Fan JL, Gong X, Huang BY, Song M, Liu T, Tian JM. Densification behavior of nano crystalline W-Ni-Fe composite powders prepared by sol-spray drying and hydrogen reduction process. J Alloys Compd 2010;489:188-94.

[7] Kamal SSK, Sahoo PK, Vimala J, Shanker B, Ghosal P, Durai L. Synthesis of high purity tungsten nano particles from tungsten heavy alloy scrap by selective precipitation and reduction route. J Alloys Compd 2016;678:403-9.

[8] Dincer O, Pehlivanoglu MK, Caliskan NK, Karakaya I, Kalkanli A. Processing and microstructural characterization of liquid phase sintered tungsten-nickel-cobalt heavy alloys. Int J Refract Met Hard Mater 2015;50:106-12.

[9] Ding L, Xiang DP, Li YY, Zhao YW, Li JB. Phase, microstructure and properties evolution of fine-grained W-Mo-Ni-Fe alloy during spark plasma sintering. Mater Des 2012;37:8-12.

[10] Ding L, Xiang DP, Pan YL, Li YY. Mechanical properties and microstructural evolution of Mo-Co-co strengthened W-Ni-Fe alloys by spark plasma sintering. J Alloys Compd 2017;712:593-8.

[11] Kocich R, Kuncicka L, Dohnalik D, Machackova A, Sofer M. Cold rotary swaging of a tungsten heavy alloy: numerical and experimental investigations. Int J Refract Met Hard Mater 2016;61:264-72.

[12] Caliskan NK, Durlu N, Bor S. Swaging of liquid phase sintered 90W-7Ni-3Fe tungsten heavy alloy. Int J Refract Met Hard Mater 2013;36:260-4.

[13] Yu Y, Zhang W, Chen Y, Wang E. Effect of swaging on microstructure and mechanical properties of liquid-phase sintered 93W-4.9(Ni, Co)-2.1Fe alloy. Int J Refract Met Hard Mater 2014;44:103-8.

[14] Chen CL, Huang CL. Milling media and alloying effects on synthesis and characteristics of mechanically alloyed ODS heavy tungsten alloys. Int J Refract Metals Hard Mater 2014;44:19-26.

[15] Kiran UR, Panchal A, Kumar MP, Sankaranarayana M, Rao GVSN, Nandy TK. Refractory metal alloying: a new method for improving mechanical properties of tungsten heavy alloys. J Alloys Compd 2017;709:609-19.

[16] Bose A, German RM. Microstructural refinement of W-Ni-Fe heavy alloys by alloying additions. Metall Trans A 1989;19:3100-3.

[17] Wei Z, Yu J, Hu S, Li Y. Influence of microstructure on adiabatic shear localization of pre-twisted tungsten heavy alloys. Int J Impact Eng 2000;24:747-58.

[18] Luo R, Huang D, Yang M, Tang E, Wang M, He L. Penetrating performance and "self-sharpening" behavior of fine-grained tungsten heavy alloy rod penetrators. Mater Sci Eng A 2016;675:262-70.

[19] Levin ZS, Ted Hartwig K. Hardness and microstructure of tungsten heavy alloy subjected to severe plastic deformation and post-processing heat treatment. Mater Sci Eng A 2015;635:94-101.

[20] Yu Y, Hu H, Zhang W, Xu X. Microstructure evolution and recrystallization after annealing of tungsten heavy alloy subjected to severe plastic deformation. J Alloys Compd 2016;685:971-7.

[21] Liu G, Zhang GJ, Jiang F, Ding XD, Sun YJ, Sun J, et al. Nano structured high strength molybdenum alloys with unprecedented tensile ductility. Nat Mater 2013;12:344-50.

[22] Kiran UR, Panchal A, Sankaranarayana M, Rao GVSN, Nandy TK. Effect of alloying addition and microstructural parameters on mechanical properties of 93% tungsten heavy alloys. Mater Sci Eng A 2015;640:82-90.

[23] Fan JL, Gong X, Huang BY, Song M, Liu T, Qi MG, et al. Dynamic failure and adiabatic shear bands in fine-grain 93W-4.9Ni-2.1Fe alloy with Y_2O_3 addition under lower high-strain-rate (HSR) compression. Mech Mater 2010;42:24-30.

[24] Li C, Wang Y, Ma S, Yang X, Li J, Zhou Y, et al. Densification, microstructural evolutions of 90W-7Ni-3Fe tungsten heavy alloys during laser melting deposition process. J Refract Met Hard Mater 2020;91:105254.

[25] Velo IL, Gotor FJ, Alcala MD, Real C, Cordoba JM. Fabrication and characterization of WC-HEA cemented carbide based on the FeNiCoCrMn high entropy alloy. J Alloys Compd 2018;746:1-8.

[26] Zhang Y, Guo S, Liu CT, Yang X. High-entropy alloys. Springer; 2016.

[27] Zhang Y, Zuo TT, Tang Z, Gao MC, Dahmen KA, Liaw PK, et al. Microstructures and properties of high-entropy alloys. Prog Mater Sci 2014;61:1-93.

[28] Tsai MH, Yeh J-W. High-entropy alloys: a critical review. Mater Res Lett 2014;2:107-23.

[29] Liu B, Wang J, Chen J, Fang Q, Liu Y. Ultra-high strength TiC/ refractory high-entropy-alloy composite prepared by powder metallurgy. J Occup Med 2017;69:651-6.

[30] Zhu G, Liu Y, Ye J. Fabrication and properties of Ti(C,N)-based cermets with multi-component AlCoCrFeNi high-entropy alloys binder. Mater Lett 2013;113:80-2.

[31] Upadhyaya A. Processing strategy for consolidating tungsten heavy alloys for ordnance applications. Mater Chem Phys 2001;67:101-10.

[32] Bose A, Sadangi R, German RM. A review on alloying in tungsten heavy alloys. Suppl Proc 2012:453-69.

[33] Chen CS, Yang CC, Chai HY, Yeh JW, Chau JLH. Novel cermetmaterial of WC/multi-element alloy. Int J Refract Met Hard Mater 2014;43:200-4.

[34] He ZW, Wang MZ, Hao XL, Zou Q, Zhao YC. Novel cemented carbide produced with TiN0.3 and high-entropy alloys. Rare Met 2017;36:494-500.

[35] Hamid ZA, Moustafa SF, Daoush WM, Mouez FA, Hassan M. Fabrication and characterization of tungsten heavy alloys using chemical reduction and mechanical alloying methods. J Appl Sci 2013;3:15-27.

[36] Zhigang ZF. Sintering of advanced materials: fundamentals and processes. Woodhead Publishing ltd; 2010.

[37] German RM, Bose A, Mani SS. Sintering time and atmosphere influences on the microstructure and mechanical properties of tungsten heavy alloys. Metall Trans A 1992;23:211-9.

[38] Zhang S, Zhu Q, Li Q, Ji W, Wang W, Fu Z. Ultrafine-grained tungsten heavy alloy prepared by high-pressure spark plasma sintering. Materials 2022;15:6168.

[39] Satyanarayana PV, Sokkalingam R, Jena PK, Sivaprasad K, Prashanth KG. Tungsten matrix composite reinforced with CoCrFeMnNi high-entropy alloy: impact of processing routes on microstructure and mechanical properties. Metal 2019.

[40] Chu C, Chen W, Chen Z, Jiang Z, Wang H, Fu Z. Microstructure and mechanical behavior of FeNiCoCr and FeNiCoCrMn high-entropy alloys fabricated by powder metallurgy. Acta Metall Sin 2021;34:445-54.

[41] German RM, Suri P, Park SJ. Review: liquid phase sintering. J Mater Sci 2009;44:1-39.

[42] Zhou S, Liang YJ, Zhu Y, Jian R, Wang B, Xue Y, et al. High entropy alloy: a promising matrix for high-

performance tungsten heavy alloys. J Alloys Compd 2019;777:1184—90.

[43] Jian R, Wang L, Zhou S, Zhu Y, Liang YJ, Wang B, et al. Achieving fine-grain tungsten heavy alloys by selecting a high entropy alloy matrix with low W grain growth rate. Mater Lett 2020;278:128405—8.

[44] Soares GC, Patnamsetty M, Peura P, Hokka M. Effects of adiabatic heating and strain rate on the dynamic response of a CoCrFeMnNi high-entropy alloy. J Dyn Beh Mater 2019;5:320—30.

[45] Yasnikov IS, Kaneko Y, Uchida M, Vinogradov A. The grain size effect on strain hardening and necking instability revisited from the dislocation density evolution approach. Mater Sci Eng 2022;831:142330—41.

Malik Adeel Umer received his PhD from KAIST in 2015. Since then, he has been serving as a faculty member at NUST, Pakistan. His research interests are ceramics and metal-matrix composites for wear and structural applications. He is supervising research on the fabrication, optimization, and industrial applications of high entropy alloy composites and cermets for wear and structural applications.